

## 2 **Collide and Conquer: Constraints on Simplified Dark** 3 **Matter Models using Mono- $X$ Collider Searches**

---

4 **A. J. Brennan,<sup>a,1</sup> M. F. McDonald,<sup>a</sup> J. Gramling<sup>b</sup> and T. D. Jacques<sup>c</sup>**

5 <sup>a</sup>*The University of Melbourne, Parkville 3010, Australia*

6 <sup>b</sup>*Université de Genève, Quai E. Ansermet 24, 1211 Genève 4, Switzerland*

7 <sup>c</sup>*SISSA/ISAS, via Bonomea 265, 34136 Trieste, Italy*

8 *E-mail:* [amelia.brennan@coepp.org.au](mailto:amelia.brennan@coepp.org.au), [millie.mcdonald@coepp.org.au](mailto:millie.mcdonald@coepp.org.au),  
[johanna.gramling@cern.ch](mailto:johanna.gramling@cern.ch), [thomas.jacques@sissa.it](mailto:thomas.jacques@sissa.it)

9 **ABSTRACT:** The use of simplified models of dark matter is becoming increasingly prevalent  
10 in collider searches, and while early Run II results are beginning to appear, we look to see  
11 what further information can be extracted from Run I results. We consider three ‘standard’  
12 simplified models that couple quarks to fermionic singlet dark matter: an  $s$ -channel vector  
13 mediator with vector or axial-vector couplings, and a  $t$ -channel scalar mediator. Upper lim-  
14 its on the couplings are calculated, and compared across three alternate channels, namely,  
15 mono-jet, mono- $Z$  (leptonic) and mono- $W/Z$  (hadronic). The strongest limits are observed  
16 in the mono-jet channel, however the computational simplicity, and absence of significant  
17  $t$ -channel model width effects, in the mono-boson channels make these a straightforward  
18 and fast alternative.

---

<sup>1</sup>Corresponding author.

---

19	<b>Contents</b>	
20	<b>1 Introduction</b>	<b>2</b>
21	<b>2 Simplified Model Phenomenology</b>	<b>3</b>
22	2.1 Model Descriptions	3
23	2.2 The Mono- $X + E_{\text{T}}^{\text{miss}}$ Signature	4
24	2.3 Mass and Coupling Points	5
25	2.4 Treatment of the width	5
26	<b>3 Recasting mono-<math>X</math> constraints</b>	<b>7</b>
27	3.1 Signal Simulation	8
28	3.1.1 Parton Matching Scheme	9
29	3.2 Mono-jet Constraints	9
30	3.3 Mono- $Z(\text{lep})$ Constraints	10
31	3.4 Mono- $W/Z(\text{had})$ Constraints	11
32	<b>4 Results and Discussion</b>	<b>12</b>
33	4.1 Limits on the coupling $\sqrt{g_q g_\chi}$	12
34	4.1.1 Mono-jet channel	13
35	4.1.2 Mono- $Z(\text{lep})$ channel	13
36	4.1.3 Mono- $W/Z(\text{had})$ channel	14
37	4.2 Comparison with Relic Density Constraints	14
38	4.3 Comparison with Direct Detection Constraints	20
39	4.4 Discussion	20
40	<b>5 Conclusion</b>	<b>21</b>
41	<b>6 Acknowledgements</b>	<b>21</b>
42	<b>A Limit setting strategy</b>	<b>21</b>
43	A.1 Nominal Values	21
44	A.2 Uncertainty Estimation	21
45	<b>B Validation of signal simulation and event selection procedures</b>	<b>22</b>
46	B.1 Monojet Channel	22
47	B.2 Mono- $Z(\text{lep})$ Channel	23
48	B.3 Mono- $W/Z(\text{had})$ Channel	24

---

# 1 Introduction

Simplified models have emerged as a powerful tool for the interpretation of collider, direct and indirect detection signals of dark matter (DM). Previously, ATLAS and CMS searches for DM were conducted within the context of both Effective Field Theories (EFTs) [1, 5, 32, 33] and full UV-complete theories such as Supersymmetry [10–12, 40]. The latter approach, though well-motivated, is typified by a broad parameter space and generally yields results which are insensitive to the wider class of DM models. EFT constraints, in comparison, are applicable to a broad range of models and rely on the specification of only a small set of parameters, namely the suppression scale,  $M_\star$ , and the DM mass,  $m_{\text{DM}}$  [25]. In the EFT framework, interactions between the dark and Standard Model (SM) sector are parametrised by a set of higher-dimensional effective operators, that arise when the mass of the mediating particle is assumed to be significantly larger than the momentum transferred in a given interaction. Where this is not the case, the EFT prescription can produce constraints which detour dramatically from those of the associated UV-complete model [24–28]. This is not so important in direct detection experiments where the momentum transferred in the scattering of DM particles with heavy nuclei is generally of the order of tens of MeV [13, 14], or in indirect searches where the annihilations of non-relativistic DM particles in the galactic halo occur with momentum transfers of order  $m_{\text{DM}}$ . However, for hadron collider searches - where the accessible center of mass energy of two colliding baryons may be sufficient to produce the mediator on-shell - the range of validity of the EFT prescription is significantly diminished. Indeed, recent works have shown the EFT approach to be problematic in certain cases for the interpretation of data collected during the  $\sqrt{s} = 8$  TeV Run I of the Large Hadron Collider (LHC) [15–17]. In light of this, simplified models have become the preferred tool for the interpretation of collider DM searches [18, 31, 53, 55, 56].

In a nutshell, a simplified model (SiM) arises when the heavy mediator which was integrated out in the EFT framework is reintroduced. Like EFTs, SiMs admit the comparison of results obtained in the different avenues of dark matter study [] and are defined by a relatively small set of parameters - namely  $m_{\text{DM}}$ , the mass of the mediator  $M_{\text{med}}$ , and the SM-mediator and DM-mediator coupling strengths,  $g_q$  and  $g_\chi$  (or  $g_{q\chi}$  in the case of a single, SM-DM-mediator coupling). Unlike EFTs, constraints calculated within the context of a SiM are valid across a broad energy range.

In this paper, we examine a phenomenologically distinct set of SiMs. In particular, we place constraints on the SiMs corresponding to the simplest UV-completions of the D5 (vector) and D8 (axial-vector) effective operators in the  $s$ -channel<sup>1</sup>. We also include a case in which a scalar mediator is exchanged in the  $t$ -channel, motivated by its analog of squark exchange in Supersymmetry. In the heavy mediator limit, this model can be expressed as a combination of operators D5 to D8 via a Fierz transformation.

---

<sup>1</sup>The D5 and D8 operators form a nice starting point in the analysis of SiMs as they have been studied exhaustively in the past (see refs. [1, 4, 5, 7, 15–17, 32, 33] among others). This attention is motivated by the fact that collider limits for the D5 (D8) operator can be readily transformed into limits on spin-independent (spin-dependent) DM-nucleon scattering and vice versa.

The models are constrained using public results from mono- $X$  + missing transverse energy ( $E_T^{\text{miss}}$ ) searches conducted by the ATLAS Collaboration. Specifically we focus on searches where  $X$  is either a parton (manifesting in the detector as a narrow-radius jet), a leptonically-decaying  $Z$  boson, or a hadronically-decaying  $W$  or  $Z$  boson (manifesting as a large-radius jet). The purpose of this work is to strengthen existing SiM limits (see for e.g. [23, 57]) using the full  $20.3 \text{ fb}^{-1}$  of Run I ATLAS data, and to explore an enhanced phase space with respect to the mediator and DM masses and the relative strength of the couplings to the visible and dark sectors. We choose to treat the mediator width as the minimal value naturally arising, which is more realistic than a fixed width. We extend the study by providing a cross-check and comparison of the performance of the three targeted collider detection channels, and compare against relic density and direct detection constraints.

The remainder of the paper is organised as follows. Section 2 contains a compendium of the SiMs chosen for analysis and the associated collider phenomenology. Section 3 outlines the techniques used to recast mono- $X$  +  $E_T^{\text{miss}}$  limits on the visible cross-section for any new physics process into constraints on SiMs, and specifically on the couplings  $g_q$  and  $g_\chi$ . Lastly, our results are presented in section 4 along with a discussion of the implications of this work. Appendices A and B include details of the limit setting and analysis validation procedures.

## 2 Simplified Model Phenomenology

### 2.1 Model Descriptions

We begin with a short set of assumptions: that the DM particle,  $\chi$ , is a weakly interacting Dirac fermion, that it is a singlet under the SM, and that it is the lightest stable new particle. Additionally the new sector is assumed to couple only to the SM quarks; while possible coupling to SM leptons e.g. [26] or gluons e.g. [59] has been studied elsewhere, it is beyond the scope of this paper. The nature of the mediating particle then results from these assumptions: in the  $s$ -channel it is chosen to be a vector particle and must also be a SM singlet, denoted  $\xi$ , while in the  $t$ -channel it is identified as scalar and is necessarily charged and coloured, and labelled  $\phi$ .

The  $s$ -channel models chosen for analysis are characterised by vector ( $sV$ ) or axial-vector ( $sA$ ) couplings to both the dark and SM sectors. They are described by the following interaction Lagrangians:

$$\mathcal{L}_{sV} \supset -\xi_\mu \left[ \sum_q g_q \bar{q} \gamma^\mu q - g_\chi \bar{\chi} \gamma^\mu \chi \right], \quad (2.1)$$

$$\mathcal{L}_{sA} \supset \xi_\mu \left[ \sum_q g_q \bar{q} \gamma^\mu \gamma_5 q - g_\chi \bar{\chi} \gamma^\mu \gamma_5 \chi \right], \quad (2.2)$$

where the sum is over all quarks. For the couplings  $g_q$  and  $g_\chi$  to remain within the perturbative regime, they are required to satisfy  $g_q, g_\chi \leq 4\pi$ , though stronger perturbativity requirements do exist [15].

The  $t$ -channel model considered in this paper (abbreviated  $tS$ ) is characterised by a scalar mediator and is motivated by analogy with a common aspect of Supersymmetric models: neutralino DM interacting with the SM sector via  $t$ -channel exchange of a squark [20]. Note that in this Supersymmetric scenario the DM particle is a Majorana fermion. The collider phenomenology of SiMs in which  $\chi$  is of Majorana type is kinematically identical to the corresponding Dirac cases (requiring multiplication of the cross-section by a simple factor in order to compute limits) and so are not covered here<sup>2</sup>. The exception to this rule is the  $s$ -channel vector mediator model, which vanishes if  $\chi$  is a Majorana fermion [21].

In the  $tS$  model, the mediator is allowed to couple to either the left or right-handed quarks as an SU(2) doublet or singlet respectively. Since the LHC is insensitive to the chirality of the quarks, we assume for simplicity that  $\phi$  couples to the left-handed quarks only, and is itself an SU(2) doublet, allowing radiation of a  $W$  boson. To avoid different couplings to quarks of different generations, and to remain in step with the DM forum recommendations [53], we include three generations of mediator  $\phi$ , with equal masses and couplings. The interaction Lagrangian for this model is then:

$$\mathcal{L}_{tS} \supset \sum_Q g_{q\chi} \bar{Q} P_R \phi \chi + \text{h.c.}, \quad (2.3)$$

where the sum is over the three quark doublets,  $g_{q\chi}$  is the scalar coupling of the incoming quark,  $\phi$  and  $\chi$ , and  $P_R$  is the usual chiral projection operator. Should  $\phi$  have a subscript  $Q$  here?

## 2.2 The Mono- $X + E_T^{\text{miss}}$ Signature

The mono- $X + E_T^{\text{miss}}$  (abbreviated to mono- $X$ ) is a popular collider signal in the search for new physics, particularly in the search for dark matter. Since DM particles are not expected to interact with detector material, they appear as missing transverse energy when balanced against a visible object,  $X$ , that is radiated from the initial or intermediate state (where the latter is permitted in the  $t$ -channel model). For the  $s$ -channel SiMs discussed above, only initial-state radiation is permitted; see figs. 1a and 1b for examples. For the  $tS$  model, radiation of a gluon or electroweak (EW) boson is permitted both from initial state partons (fig. 1c) or from the mediator (fig. 1d).

The most likely scenario at the LHC is production of a jet alongside the invisible  $\chi$  pair, as a result of the strong coupling and prevalence of partons in the initial state. However, to fully exploit the potential of the ATLAS detector to record and identify a vast array of particle types, we can include the alternative mono- $W/Z$  channels to potentially glean further information. We can take advantage of the relative cleanliness and simplicity of leptons in the leptonically-decaying mono- $Z(\rightarrow \ell^+ \ell^-)$  channel, or the large hadronic branching fraction, and developing techniques to identify jets resulting from EW bosons, in the hadronically-decaying mono- $W/Z(\rightarrow jj)$  channel<sup>3</sup>. In both cases, the large multi-jet

<sup>2</sup>The exception being in the validation of the mono- $Z(\text{lep})$  channel, see Sec. B.2.

<sup>3</sup>In addition, one of the first Run II dark matter search results from ATLAS was from this channel [60], released during the preparation of this paper.

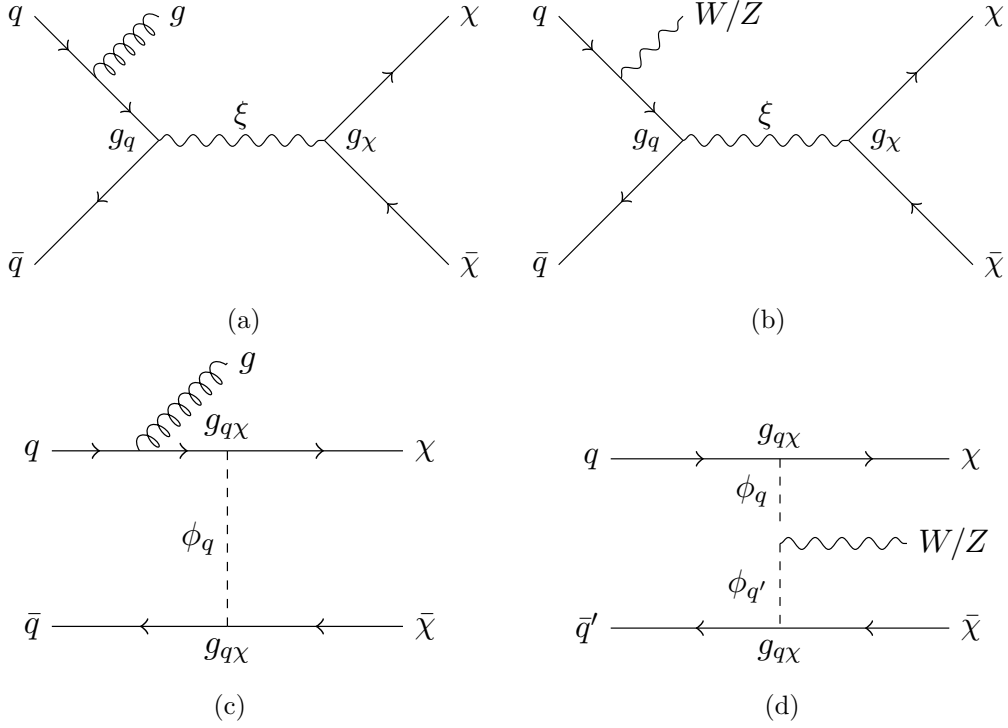


**Figure 1:** Representative dark matter pair-production processes with a gluon or  $W/Z$  boson in the final state for the  $s$ -channel (a,b) and  $t$ -channel (c,d) models.

background is reduced, and complications in jet production such as parton-matching can be ignored, making these an interesting alternative where speed, efficiency and a reduction in jet-associated uncertainties may make up for the loss in sensitivity.

### 2.3 Mass and Coupling Points

A representative set of dark matter and mediator masses, listed in table 1, are chosen for study in each detection channel. DM masses of 3, 30 and 300 GeV were also included in the mono- $Z$ (lep) channel, where ease of production can afford higher granularity. All  $(m_\chi, M_{\text{med}})$  combinations are permitted in the  $sV$  and  $sA$  models, while in the  $tS$  model  $M_{\text{med}}$  must be greater than  $m_\chi$  to ensure stability of the DM particle. The couplings  $g_q$  and  $g_{q\chi}$  are set to unity, while the DM-mediator coupling in the  $s$ -channel models,  $g_\chi$ , was varied from 0.2 to 5. The mediator masses are chosen to cover a broad range of parameter space and to coincide with predominantly three regimes: (near-)degenerate ( $M_{\text{med}} \approx m_\chi$ ), on-shell ( $M_{\text{med}} \geq 2m_\chi$ ) and off-shell ( $M_{\text{med}} < 2m_\chi$ ).

### 2.4 Treatment of the width

An important factor when considering SiMs is to ensure the mediator width is treated appropriately, as it impacts both the cross-section calculation and, in some cases, the kinematic behaviour of the model.

$m_\chi$ [GeV]	$M_{\text{med}}$ [GeV]	s-channel		t-channel
		$g_q$	$g_\chi$	$g_{q\chi}$
1, (3), 10, (30), 100, (300), 1000	1, 2, 10, 20, 100, 200, 1000, 2000	1	0.2, 0.5, 1, 2, 5	1

**Table 1:** Mass and coupling points chosen for the analysis of simplified dark matter models. Values in brackets are only included in the mono- $Z(\text{lep})$  channel. The mediator masses are primarily representative of three regimes: (near-)degenerate ( $M_{\text{med}} \approx m_\chi$ ), on-shell ( $M_{\text{med}} \geq 2m_\chi$ ) and off-shell ( $M_{\text{med}} < 2m_\chi$ ). For the  $t$ -channel model,  $M_{\text{med}} > m_\chi$  is required to ensure stability of the DM particle.

176 Following the DM Forum recommendations [53], we use the minimal width, allowing  
177 coupling to all kinematically accessible quarks. We assume minimal flavour violation, which  
178 implies a universal coupling to all quark flavours. The minimum width for each model is  
179 given by:

$$\begin{aligned} \Gamma_{sV} = & \frac{g_\chi^2 M}{12\pi} \left(1 + \frac{2m_\chi^2}{M^2}\right) \left(1 - \frac{4m_\chi^2}{M^2}\right)^{\frac{1}{2}} \Theta(M - 2m_\chi) \\ & + \sum_q \frac{g_q^2 M}{4\pi} \left(1 + \frac{2m_q^2}{M^2}\right) \left(1 - \frac{4m_q^2}{M^2}\right)^{\frac{1}{2}} \Theta(M - 2m_q) \end{aligned} \quad (2.4)$$

$$\begin{aligned} \Gamma_{sA} = & \frac{g_\chi^2 M}{12\pi} \left(1 - \frac{4m_\chi^2}{M^2}\right)^{\frac{3}{2}} \Theta(M - 2m_\chi) \\ & + \sum_q \frac{g_q^2 M}{4\pi} \left(1 - \frac{4m_q^2}{M^2}\right)^{\frac{3}{2}} \Theta(M - 2m_q) \end{aligned} \quad (2.5)$$

$$\begin{aligned} \Gamma_{tS} = & \sum_q \frac{g_{q\chi}^2 M}{16\pi} \left(1 - \frac{m_q^2}{M^2} - \frac{m_\chi^2}{M^2}\right) \\ & \times \sqrt{\left(1 - \frac{m_q^2}{M^2} + \frac{m_\chi^2}{M^2}\right)^2 - 4 \frac{m_\chi^2}{M^2}} \Theta(M - m_q - m_\chi) \end{aligned} \quad (2.6)$$

180 It is possible that the mediator may decay to other SM or BSM particles [31], but this  
181 is not expected to have a large effect on the kinematic distribution as long as the width  
182 remains relatively small [53]. The generator treatment of the mediator as a Breit-Wigner  
183 propagator, rather than a true kinetic propagator, breaks down for large widths [57].

184 To simplify the procedure, we can take advantage of the fact that (with the notable  
185 exception of the  $tS$  model in the mono-jet channel) for each point in  $(m_\chi, M_{\text{med}})$  phase  
186 space, the mediator width (and therefore the couplings) do not greatly affect each model's

kinematic behaviour. This is demonstrated in fig. 2, where for the  $sV$  (representing both the  $sV$  and  $sA$  models) and  $tS$  models, we plot a simplified  $E_T^{\text{miss}}$  distribution, as a proxy for the full selection in each analysis, for two mass points and a demonstrative set of couplings such that  $\Gamma < M_{\text{med}}/2$ . The  $E_T^{\text{miss}}$  distribution is predominantly independent of the mediator width for the  $s$ -channel models in the mono-jet channel, and all models in the mono- $Z(\text{lep})$ <sup>4</sup> channel. However, there is a clear variation in the kinematic behaviour of the  $tS$  model in the mono-jet channel, which can be attributed to additional diagrams (accessible only in this channel) featuring a gluon in the initial state and subsequently allowing the mediator to go on-shell. In this scenario, when the resulting quark and DM particle are both small compared to the mediator mass, they share equally its energy leading to a peak in the  $E_T^{\text{miss}}$  distribution at approximately half the mediator mass.

In the cases where the model behaviour is independent of the width, we can greatly simplify the calculations by assuming the impact of the selection cuts in each channel is unchanged by the couplings. In this case, the following relations hold [57]:

$$\sigma \propto \begin{cases} g_q^2 g_\chi^2 / \Gamma & \text{if } M_{\text{med}} \geq 2m_{\text{DM}} \\ g_q^2 g_\chi^2 & \text{if } M_{\text{med}} < 2m_{\text{DM}} \end{cases} \quad (2.7)$$

in the  $sV$  and  $sA$  models, and

$$\sigma \propto g_{q\chi}^4 \quad (2.8)$$

in the  $tS$  model. When valid, these approximations allow us to greatly simplify our limit calculations, and for this reason, we restrict our primary results to regions of parameter space where  $\Gamma/M < 0.5$ . See app. A for further details of the limit-setting calculation.

A proper study of the  $tS$  model within the mono-jet channel, where altering the coupling can lead to changed kinematic behaviour, has been performed elsewhere [23], and requires the production of individual samples for each coupling point. This, combined with the challenges associated with including differing orders of  $\alpha_s$ , make the generation process computationally expensive compared to the mono- $Z(\text{lep})$  and mono- $W/Z(\text{had})$  channels. We therefore exclude an analysis of the  $tS$  model in the mono-jet channel in this work.

### 3 Recasting mono- $X$ constraints

The procedure for recasting existing mono- $X$  analyses to obtain SiM constraints follows a simple cut-and-count methodology. Firstly, signal events are simulated (described below in section 3.1) with object  $p_T$  smearing applied to approximate the detection efficiency of the ATLAS detector,  $\epsilon$ . The event selection criteria of the mono- $X$  analysis of interest is then applied to the simulated signal samples. Events surviving the selection criteria are counted to determine the likelihood of a dark matter event being observed (referred

---

<sup>4</sup>In this discussion, the mono- $W/Z(\text{had})$  channel can be assumed to follow the same logic as for the mono- $Z(\text{lep})$  channel.





**Figure 2:** The  $E_T^{\text{miss}}$  distribution of the  $sV$  and  $tS$  models in the mono-jet and mono- $Z(\text{lep})$  channels, for some demonstrative masses. The parameter  $\mu$  is defined as  $\Gamma/M_{\text{med}}$ , and is used to demonstrate the impact of a changing width; in particular, the  $tS$  model in the mono-jet channel shows clear width-dependence. The widths are obtained with couplings of 0.1, 1, and 5 where  $\mu < 0.5$  remains true.

to as the acceptance,  $\mathcal{A}$ ), which is then used in combination with channel-specific model-independent limits on new physics events to limit the parameter phase space of a given model. For a comprehensive description of the recasting procedure, see appendix A.

In this paper, mono-jet constraints are derived from a search for new phenomena conducted by the ATLAS Collaboration using  $pp$  collisions at  $\sqrt{s} = 8$  TeV as described in ref. [41]. Similarly, the leptonic mono- $Z$  and hadronic mono- $W/Z$  constraints are derived from ATLAS dark matter searches that were optimised for the D1, D5 and D9 effective operators [47, 48]. These analyses are described in further detail in sections 3.2, 3.3 and 3.4 respectively.

### 3.1 Signal Simulation

Monte Carlo simulated event samples are used to model the expected signal for each channel and for each SiM. Leading order matrix elements for the process  $pp \rightarrow X + \chi\bar{\chi}$  (where

<sup>230</sup>  $X$  is specifically one or two jets<sup>5</sup>, a  $Z(\rightarrow \ell^+\ell^-)$  boson or a  $W/Z(\rightarrow jj)$  boson) are first  
<sup>231</sup> simulated using MADGRAPH5\_aMC@NLO v2.2.2 [49] with the MSTW2008lo68cl PDF [50].  
<sup>232</sup> During this stage, the renormalisation and factorisation scales are set to the default sum  
<sup>233</sup> of  $\sqrt{m^2 + p_T^2}$  for all particles in the final state. Showering and hadronisation are then  
<sup>234</sup> performed by PYTHIA 8.201 [58] with the appropriate PDF and using the ATLAS UE  
<sup>235</sup> Tune AU2-MSTW2008LO [51]. Reconstruction of small-radius jets (from hereon referred  
<sup>236</sup> to just as ‘jets’) for the mono-jet channel is performed by FASTJET [63] using the anti- $k_T$   
<sup>237</sup> algorithm with radius parameter  $R = 0.4$ . Similarly, reconstruction of large-radius jets for  
<sup>238</sup> the mono- $W/Z(\text{had})$  channel is performed using the Cambridge-Aachen algorithm with  $R$   
<sup>239</sup>  $= 1.2$ . The latter channel also includes a mass-drop filtering procedure with  $\mu = 0.67$  and  
<sup>240</sup>  $\sqrt{y}$ <sup>6</sup>  $= 0.4$  (see ref. [62] for further details), which favours large- $R$  jets with two balanced  
<sup>241</sup> subjets, consistent with the decay of an EW boson to a (potentially-boosted) dijet pair.  
<sup>242</sup> Lastly, the detector response is approximated by applying a Gaussian smearing factor to  
<sup>243</sup> the  $p_T$  of all leptons and jets.

### <sup>244</sup> 3.1.1 Parton Matching Scheme

<sup>245</sup> In the ATLAS mono-jet analysis, matching of partons generated in MADGRAPH5 to jets  
<sup>246</sup> generated in PYTHIA 8 is performed using the MLM scheme [61], with two matching scales,  
<sup>247</sup> or values of ‘QCUT’, per mass/coupling point. The QCUT values span a broad kinematic  
<sup>248</sup> range in combination with a cut placed on the leading jet  $p_T$  per event to avoid double-  
<sup>249</sup> counting. This treatment aims to mitigate the impact of the matching scale on the shape  
<sup>250</sup> of the  $p_T$  and  $E_T^{\text{miss}}$  distributions; that is, to reduce the uncertainty in those areas of phase  
<sup>251</sup> space where the mediator mass is significantly larger or smaller than the QCUT value.  
<sup>252</sup> For the analysis of SiMs, we use instead a single matching scale of 80 GeV. Though not  
<sup>253</sup> ideal, this approach suitably reproduces the results of the ATLAS mono-jet analysis for  
<sup>254</sup> the masses of interest (see Sec. B.1). Importantly, it also reduces the complexity and  
<sup>255</sup> computational expense involved in estimating limits for the mono-jet channel.

<sup>256</sup> We now move to a discussion of each of the mono- $X$  channels separately.

## <sup>257</sup> 3.2 Mono-jet Constraints

<sup>258</sup> The ATLAS mono-jet +  $E_T^{\text{miss}}$  analysis [41] was originally designed to set limits on three  
<sup>259</sup> new physics scenarios, the most relevant of which is the production of WIMP DM within  
<sup>260</sup> the context of a set of effective operators. The analysis also includes a brief study of a  $Z'$   
<sup>261</sup> DM model which is analogous to our  $sV$  model.

<sup>262</sup> Signal selection is carried out based on at least one hard jet recoiling against missing  
<sup>263</sup> energy. To ensure that the correct back-to-back jet +  $E_T^{\text{miss}}$  topology is selected events are  
<sup>264</sup> required to have a leading jet,  $j_1$ , with  $p_T > 120$  GeV and  $|\eta| < 2.0$  satisfying  $p_T^{j_1}/E_T^{\text{miss}} >$   
<sup>265</sup>  $0.5$ . Surviving events must then satisfy  $|\Delta\phi(j, \vec{E}_T^{\text{miss}})| > 1.0$ , where  $j$  is any jet with  $p_T >$   
<sup>266</sup>  $30$  GeV and  $|\eta| < 4.5$ . This criterion reduces the multijet background contribution where  
<sup>267</sup> the large  $E_T^{\text{miss}}$  originates mainly from jet energy mismeasurement. Note that there is no

---

<sup>5</sup>Jets are seeded by any parton excluding the (anti-)top quark.

<sup>6</sup> $\sqrt{y} = \min(p_{T_{j_1}}, p_{T_{j_2}})\Delta R/m_{jet}$  is the momentum balance of the two leading subjets.

upper limit placed on the number of jets per event. The contribution from the dominant background processes,  $W/Z$ +jets, is managed with a veto on events containing muons or electrons with  $p_T > 7$  GeV. Lastly, nine separate signal regions are defined with increasing lower thresholds on  $E_T^{\text{miss}}$ , which range from 150 GeV to 700 GeV as shown in table 2.

The ATLAS mono-jet analysis revealed no significant deviation of observed events from the expected SM backgrounds in the Run 1 8 TeV dataset. Subsequently, model-independent limits on new physics signatures were provided in terms of the visible cross-section,  $\sigma \times \mathcal{A} \times \epsilon$ ; these are listed in table 2.

Signal Region	$E_T^{\text{miss}}$ threshold [GeV]	$\sigma \times \mathcal{A} \times \epsilon$ [fb]
SR1	150	726 (935)
SR2	200	194 (271)
SR3	250	90 (106)
SR4	300	45 (51)
SR5	350	21 (29)
SR6	400	12 (17)
SR7	500	7.2 (7.2)
SR8	600	3.8 (3.2)
SR9	700	3.4 (1.8)

**Table 2:** The ATLAS mono-jet  $E_T^{\text{miss}}$  signal regions and corresponding observed (expected) model-independent upper limits on  $\sigma \times \mathcal{A} \times \epsilon$  at 95% confidence level. Adapted from ref. [41].

The signal simulation procedure outlined in sec. 3.1 and implementation of the selection criteria discussed above were validated for the mono-jet channel via reproduction of ATLAS limits on the suppression scale,  $M_\star \equiv M_{\text{med}}/\sqrt{g_q g_\chi}$ , for the  $Z'$  model. The details of this process are contained in appendix B.1. Importantly, we observe agreement within  $\sim 12\%$  for all samples.

### 3.3 Mono- $Z(\text{lep})$ Constraints

The ATLAS mono- $Z(\rightarrow \ell^+ \ell^-) + E_T^{\text{miss}}$  analysis [47] was principally designed to constrain a set of EFT models of DM. As a secondary focus, it also includes a short study of a  $t$ -channel SiM similar to our  $tS$  model.

The selection criteria for this analysis are summarised as follows (see the paper for a full description). Electrons (muons) are required to have a  $p_T$  greater than 20 GeV, and  $|\eta|$  less than 2.47 (2.5). Two opposite-sign, same-flavour leptons are selected, and required to have invariant mass and pseudorapidity such that  $m_{\ell\ell} \in [76, 106]$  GeV and  $|\eta^{\ell\ell}| < 2.5$ . The reconstructed  $Z$  boson should be approximately back-to-back and balanced against the  $E_T^{\text{miss}}$ , ensured with the selections  $\Delta\phi(\vec{E}_T^{\text{miss}}, p_T^{\ell\ell}) > 2.5$  and  $|p_T^{\ell\ell} - E_T^{\text{miss}}|/p_T^{\ell\ell} < 0.5$ . Events containing a jet with  $p_T > 25$  GeV and  $|\eta| < 2.5$  are vetoed. Events are also vetoed if they contain a third lepton with  $p_T > 7$  GeV. The signal regions are defined by increasing lower  $E_T^{\text{miss}}$  thresholds:  $E_T^{\text{miss}} > 150, 250, 350, 450$  GeV.

294 A cut-and-count strategy is used to estimate the total observed yields and expected SM  
 295 backgrounds in each signal region. The limits on  $\sigma \times \mathcal{A} \times \epsilon$  are not publicly available, so we  
 296 take the numbers of expected and observed events, along with the associated uncertainties,  
 297 and convert these into model-dependent upper limits with a single implementation of the  
 298 HistFitter framework [54] using a frequentist calculator and a one-sided profile likelihood  
 299 test statistic (the LHC default). The results of this process are displayed in table 3. Note  
 300 that we use signal regions 1 and 2 only, as our simplified HistFitter approach is inadequate  
 301 to handle the very low statistics of signal regions 3 and 4. These upper limits are also  
 302 used for the validation of the mono- $Z(\text{lep})$  signal generation and selection procedures (see  
 303 app. B.2).

Signal Region	$E_{\text{T}}^{\text{miss}}$ threshold [GeV]	$\sigma \times \mathcal{A} \times \epsilon$ [fb]
SR1	150	1.59 (1.71)
SR2	250	0.291 (0.335)

**Table 3:** The ATLAS mono- $Z(\text{lep})$   $E_{\text{T}}^{\text{miss}}$  signal regions and corresponding observed (ex-  
 pected) model-independent upper limits on  $\sigma \times \mathcal{A} \times \epsilon$  at 95% confidence level. Adapted  
 using HistFitter from ref. [47].

### 304 3.4 Mono- $W/Z(\text{had})$ Constraints

305 The ATLAS mono- $W/Z(\text{had}) + E_{\text{T}}^{\text{miss}}$  search [48] was aimed at constraining the spin-  
 306 independent effective operators C1, D1, and D5, and the spin-dependent operator D9. The  
 307 search was originally designed to exploit the constructive interference of  $W$  boson emission  
 308 from opposite-sign up-type and down-type quarks, leading to DM production wherein the  
 309 mono- $W$  channel is dominant. Recent studies [64] have revealed this scenario to violate  
 310 gauge invariance and so we ignore it in this analysis.

311 The mono- $W/Z(\text{had})$  event selection is carried out as follows. Large-radius jets are  
 312 selected using a mass-drop filtering procedure (see sec. 3.1) to suppress non- $W/Z$  processes.  
 313 Events are required to contain at least one large- $R$  jet with  $p_{\text{T}} > 250$  GeV,  $|\eta| < 1.2$  and  
 314 a mass,  $m_{\text{jet}}$ , within a 30-40 GeV window of the  $W/Z$  mass (i.e.  $m_{\text{jet}} \in [50, 120]$  GeV).  
 315 In order to reduce the  $t\bar{t}$  and multijet backgrounds, a veto removes events containing a  
 316 small- $R$  jet with  $\Delta\phi(\text{jet}, E_{\text{T}}^{\text{miss}}) < 0.4$ , or containing more than one small- $R$  jet with  $p_{\text{T}} >$   
 317 40 GeV,  $|\eta| < 4.5$ , and  $\Delta R(\text{small-}R \text{ jet, large-}R \text{ jet}) > 0.9$ . Electrons, muons and photons  
 318 are vetoed if their  $p_{\text{T}}$  is larger than 10 GeV and they lie within  $|\eta| < 2.47$  (electrons),  
 319 2.5 (muons), 2.37 (photons). Two signal regions were defined with  $E_{\text{T}}^{\text{miss}} > 350$  GeV and  
 320  $E_{\text{T}}^{\text{miss}} > 500$  GeV.

321 The ATLAS analysis used a shape-fit of the mass distribution of the large- $R$  jet to  
 322 estimate the background yields in the two signal regions, along with the associated statis-  
 323 tical and systematic uncertainties. As in the mono- $Z(\text{lep})$  case, we do not take the shapes  
 324 into account but convert the published number of expected and observed events into upper  
 325 limits on the expected and observed number of new physics events using the HistFitter

framework. For the  $E_T^{\text{miss}} > 500$  GeV signal region, we obtain the limits shown in table 4. We do not consider the first signal region with  $E_T^{\text{miss}} > 350$  GeV in the recasting procedure, since the cut-and-count limits extracted could not be convincingly validated. The high  $E_T^{\text{miss}}$  signal region was found to be optimal for most operators studied by the ATLAS analysis.

Signal Region	$E_T^{\text{miss}}$ threshold [GeV]	$\sigma \times \mathcal{A} \times \epsilon$ [fb]
SR2	500	1.35 (1.34)

**Table 4:** The ATLAS mono- $W/Z(\text{had})$   $E_T^{\text{miss}}$  signal region considered in this work and corresponding observed (expected) model-independent upper limits on  $\sigma \times \mathcal{A} \times \epsilon$  at 95% confidence level. Adapted using HistFitter from ref. [48].

## 4 Results and Discussion

### 4.1 Limits on the coupling $\sqrt{g_q g_\chi}$

The 95% confidence level upper limits on the  $sV$  and  $sA$  model coupling combination  $\sqrt{g_q g_\chi}$ , and the  $tS$  model coupling  $g_{q\chi}$ , obtained from each of the mono- $X$  channels, are presented in figs. 3-8. These quantities were evaluated as described in appendix A, including statistical and systematic uncertainties, and correspond to the best limits of each signal region tested.

In each plot, limits are shown ranging from  $<0.01$  to the upper perturbative limit<sup>7</sup> for each coupling,  $4\pi$ ; where a limit was calculated to be larger than this, that limit is considered meaningless and the region is coloured grey. The white (hatched) regions coincide with those mass points which yield an initial (final) value of  $\sqrt{g_q g_\chi}$  or  $g_{q\chi}$  which fails to satisfy our requirement that  $\Gamma < M_{\text{med}}/2$ . (We observe that values for which the width is just within our upper validity bound of  $M_{\text{med}}/2$  may be pushed over into the invalid range with the addition of new particles, not considered here, which would serve to increase the mediator width.) When  $g_\chi/g_q = 0.2$ , only the mono-jet channel produces limits which survive this requirement, and so these are shown separately in fig. 7.

Detailed comments specific to each channel are below, however some trends are channel-independent. For the  $sV$  model, strong limits exist when  $M_{\text{med}} > 2m_\chi$  as the mediator can go on-shell, thereby enhancing the cross-section. The  $sA$  model limits show similar behaviour to the  $sV$  model except in the region where  $m_\chi \gtrsim 10 \times M_{\text{med}}$ , where the cross-section is greatly enhanced **WHY?**. The upper limit on  $\sqrt{g_q g_\chi}$  is relatively constant across values of  $g_\chi/g_q$ , as is expected when the coupling (and hence the width) has been demonstrated to have little effect on kinematic behaviour, and using the assumptions of eq. 2.7. As the ratio increases, points in the region  $M_{\text{med}} > m_\chi$  disappear as the initial condition,  $g_q = 1$ , leads to failure of the width condition. However, one could easily have chosen a

<sup>7</sup>We note that perturbativity is questionable for couplings greater than  $\sim 2 - 3$ , however  $4\pi$  is an oft-quoted hard upper limit.

smaller initial value of  $g_q$  to recover these points, and we suggest that the limits in this region would be quite similar to those seen in the  $g_\chi/g_q = 0.2$  and  $0.5$  cases.

The results are limited when  $m_\chi$  or  $M_{\text{med}}$  is large due to the suppressed cross-sections in these cases, and are expected to improve at higher centre-of-mass energies. At small DM masses with an off-shell mediator, the  $E_T^{\text{miss}}$  distribution is softer, so results in this region of phase space are limited by statistical uncertainties from being in the tail of the distribution; this region would benefit from further optimisation of event selection in analyses aimed at SiM study, as we expect to see from the upcoming Run II results.

The results are discussed according to channel below.

#### 4.1.1 Mono-jet channel

The upper limits on the coupling combination  $\sqrt{g_q g_\chi}$  of the  $sV$  and  $sA$  models, obtained in the mono-jet channel, are displayed in the left-hand column of figs. 3-6, for  $g_\chi/g_q = 0.5, 1, 2$  and  $5$  respectively. Additional results for the  $g_\chi/g_q = 0.2$  case are also shown separately in fig. 7, as these limits are only meaningful within this channel.

As expected, the mono-jet channel produces the strongest coupling limits in both  $s$ -channel models, which are better than those from the next-best mono- $Z(\text{lep})$  channel by a factor of a few. For the  $sV$  model, the weakest limits result for large  $m_\chi$  or large  $M_{\text{med}}$ , and in fact are so weak that they are pushed into the region of invalidity where  $\Gamma > M_{\text{med}}/2$ ; this is because although the acceptance is considerably higher in these regions compared to low masses, the cross section is sufficiently small that this effect prevails. Within the valid region ( $m_\chi \in [1, 100]$  GeV and  $M_{\text{med}} \in [1, 200]$  GeV), the limit on  $\sqrt{g_q g_\chi}$  generally ranges from  $0.1$  to  $0.7$ , with a handful of on-shell masses reaching a limit of  $\sim 0.05$  in the large  $g_\chi/g_q$  case. In the large  $g_\chi/g_q$  scenario, limits for  $m_\chi = 1000$  GeV start to become valid. This is because if  $\sqrt{g_q g_\chi}$  remains constant but the  $g_\chi/g_q$  increases then the value of  $g_q$  is pushed downward and so the width, which is dominated by decays to SM particles, decreases.

The  $sA$  model displays similar behaviour to the  $sV$  model except for the  $m_\chi \gtrsim 10 \times M_{\text{med}}$  region, as described above.

The uncertainties on the limits in the  $sV$  model generally range from ??% to ??%, and are dominated by X. The uncertainties for the  $sA$  model are dominated by X and are within the range  $X \sim Y\%$ .

#### 4.1.2 Mono- $Z(\text{lep})$ channel

The simplicity of the mono- $Z(\text{lep})$  channel relative to the mono-jet channel, and the speed of its production within MADGRAPH5, allowed us to study a finer granularity of points in the mass phase space. The resulting limits on the  $sV$  and  $sA$  models are shown in the central column of figs. 3-6. The behaviour of the limits as  $g_\chi/g_q$  varies is similar to that within the mono-jet channel, and overall the limits are weaker compared to that channel by a factor of a few.

The total relative uncertainties on  $\sqrt{g_q g_\chi}$  in the  $s$ -channel models are generally within 10%, but can range up to 80% in a few cases; they are dominated by X.

396 The advantage of the mono-boson channels is in the study of the  $tS$  model; since  
 397 this was not included in the mono-jet channel the strongest limits are obtained with the  
 398 mono- $Z(\text{lep})$  analysis, and are shown in the left-hand side of fig. 8. Note that the scale  
 399 here is increased by a factor of 10 from the  $s$ -channel model limits, in general the  $tS$   
 400 model limits are weaker than the corresponding  $s$ -channel points, thanks to an orders-of-  
 401 magnitude weaker cross-section and the inability of the mediator to go on-shell in this  
 402 channel. We find stronger limits for smaller  $m_\chi$  and  $M_{\text{med}}$  masses, where larger cross  
 403 sections compensate for lower acceptances at these points.

### 404 4.1.3 Mono- $W/Z(\text{had})$ channel

405 The limits on the couplings of the  $sV$ ,  $sA$  and  $tS$  models, obtained within the mono-  
 406  $W/Z(\text{had})$  channel, are shown in the right-hand column of figs. 3-8. This channel was  
 407 studied to compare with the leptonic mono- $Z(\text{lep})$  channel in particular, but a coarser  
 408 selection of masses was chosen as the limits were initially found to be somewhat weaker.  
 409 Additionally, further estimates were made: a) as the kinematic behaviour is reasonable  
 410 independent of the couplings, a single acceptance was found for each  $(m_\chi, M_{\text{med}})$  combi-  
 411 nation and applied to each value of  $g_\chi/g_q$ , and b) complete systematic uncertainties were  
 412 generated for a subset of masses and compared to those from the mono- $Z(\text{lep})$  channel;  
 413 from this comparison the mono- $Z(\text{lep})$  systematic uncertainties were multiplied by 3 and  
 414 then applied to the mono- $W/Z(\text{had})$  limits. As a result, the limits obtained in this chan-  
 415 nel are not intended to be rigorously quantitative; rather, they are used more to indicate  
 416 qualitatively how the channel compares.

417 The ATLAS mono- $W/Z(\text{had})$  analysis (and in particular the higher  $E_{\text{T}}^{\text{miss}}$  signal re-  
 418 gion) was not optimised for a SiM interpretation, and much of the phase space produced  
 419 insignificant numbers of events passing the event selection, with up to 200 thousand events  
 420 generated. Generally, the limits are a factor of a few weaker again than those from the  
 421 mono- $Z(\text{lep})$  channel, which is both consistent with the limits on the EFT models studied  
 422 in the ATLAS analyses, and expected following our use of a cut-and-count interpretation,  
 423 rather than a shape analysis, of the mono- $W/Z(\text{had})$  public results.

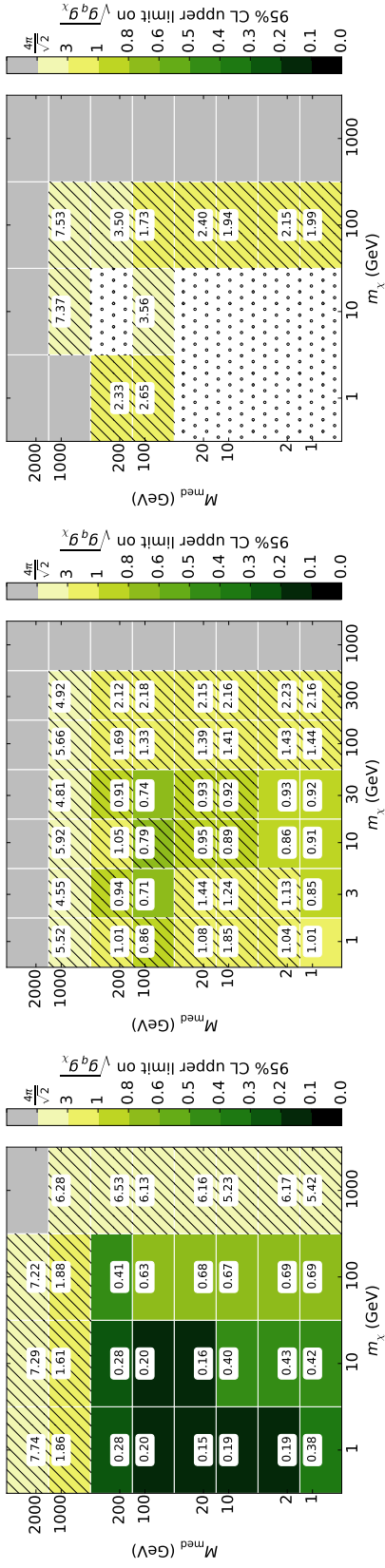
424 In some cases - most notably the  $m_\chi \gtrsim 10 \times M_{\text{med}}$  region - the limits become comparable  
 425 with the mono- $Z(\text{lep})$  channel, suggesting that more statistics and an improved treatment  
 426 of systematic uncertainties would bring these closer in line with that channel.

427 Overall, the uncertainties from this channel lie within the range XXX and are domi-  
 428 nated by Y.

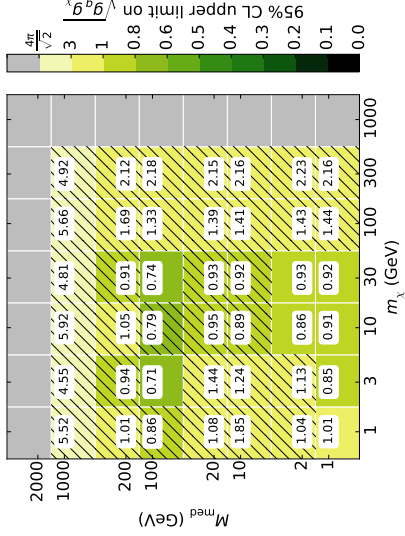
## 429 4.2 Comparison with Relic Density Constraints

430 In Figs. ?? we show lines where the constraint on the coupling corresponds to the coupling  
 431 strength that would reproduce the correct DM density if DM is a thermal relic of the  
 432 early universe. For points diagonally above and to the left of the dashed line, the LHC  
 433 constraints naively rule out the couplings leading to the correct relic density. Below and  
 434 to the right of this line the relic density coupling is still allowed.

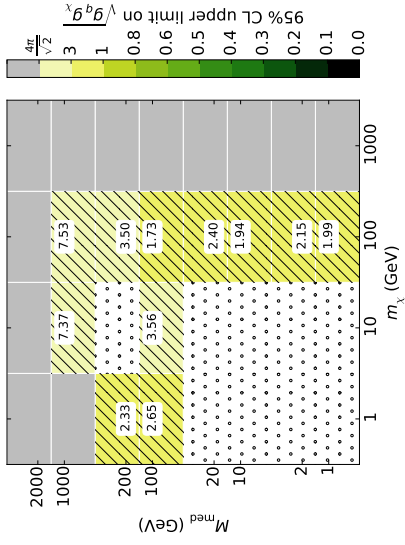




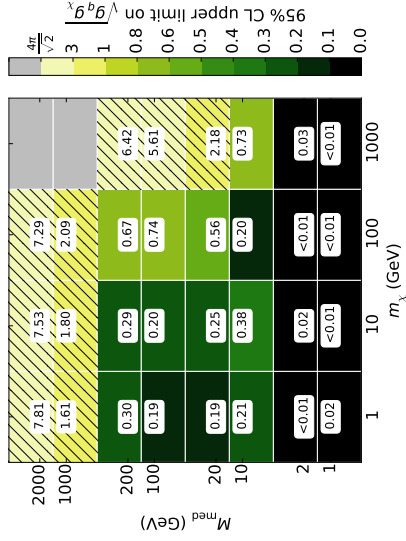
(a)  $sV$  model,  $g_X/g_q = 0.5$ , mono-jet channel.



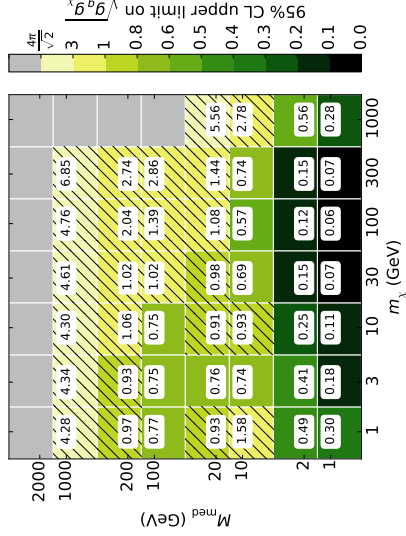
(b)  $sV$  model,  $g_X/g_q = 0.5$ , mono- $Z$  channel.



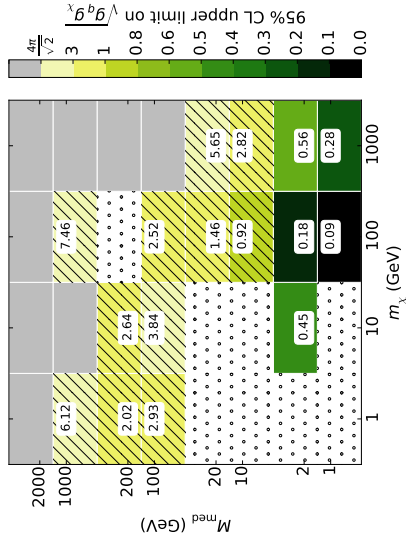
(c)  $sV$  model,  $g_X/g_q = 0.5$ , mono- $W/Z$  channel.



(d)  $sA$  model,  $g_X/g_q = 0.5$ , mono-jet channel.



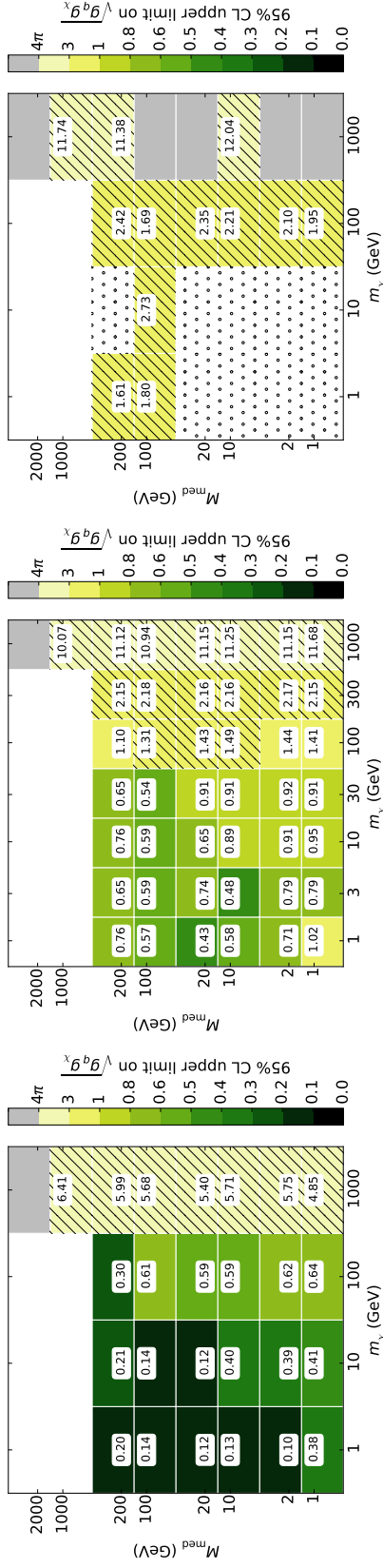
(e)  $sA$  model,  $g_X/g_q = 0.5$ , mono- $Z$  channel.



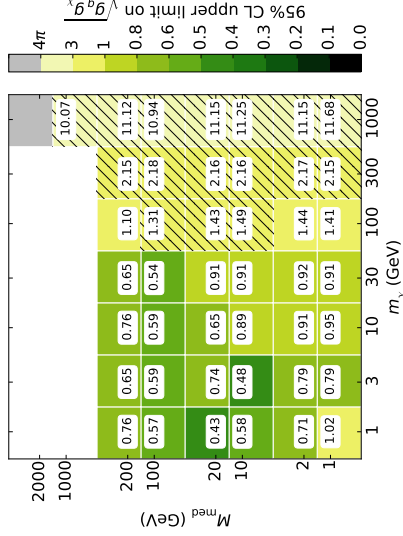
(f)  $sA$  model,  $g_X/g_q = 0.5$ , mono- $W/Z$  channel.

**Figure 3:** Upper limits on the coupling for the  $s$ -channel models in the mono-jet (left), mono- $Z$ (lep) (centre) and mono- $W/Z$ (had) (right) channels, for  $g_X/g_q = 0.5$ . The grey region represents the phase space where no meaningful limit was obtained. The hatched region represents a limit which leads to a width greater than  $M_{\text{med}}/2$ , so the validity of the calculation begins to fail. The dotted region represents phase space where insufficient statistics were available.

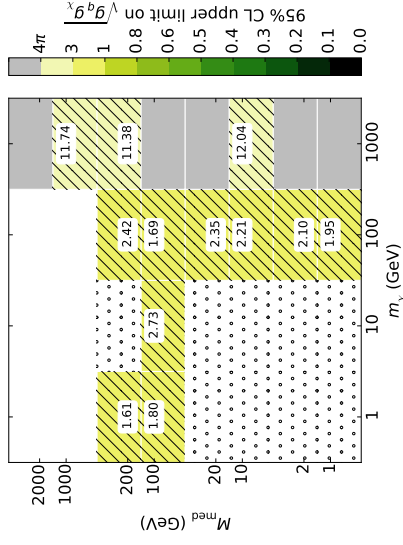




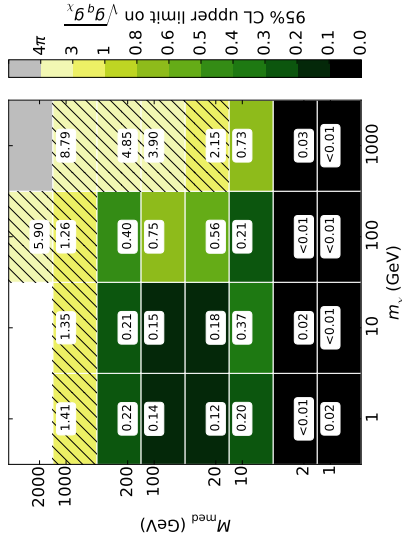
(a)  $sV$  model,  $g_\chi/g_q = 1$ , mono-jet channel.



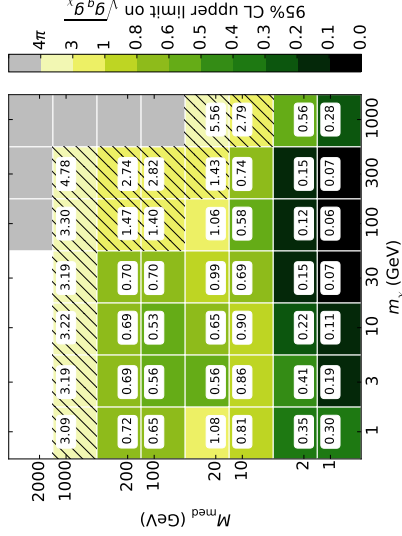
(b)  $sV$  model,  $g_\chi/g_q = 1$ , mono- $Z$  channel.



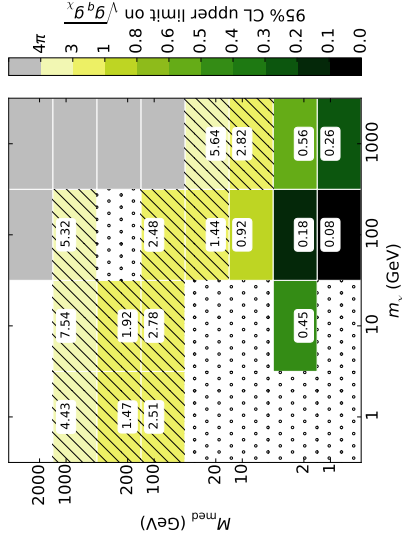
(c)  $sV$  model,  $g_\chi/g_q = 1$ , mono- $W/Z$  channel.



(d)  $sA$  model,  $g_\chi/g_q = 1$ , mono-jet channel.

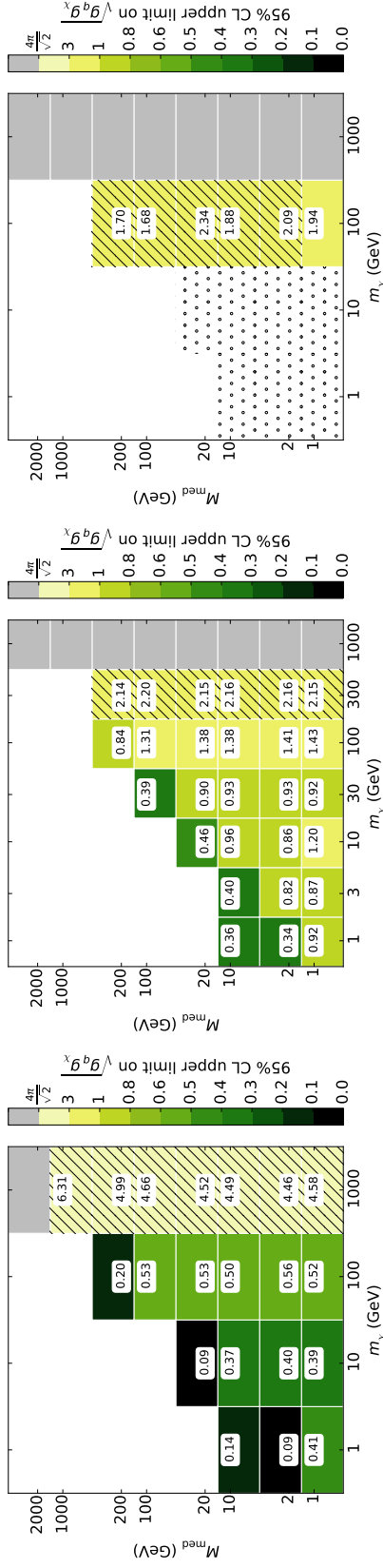


(e)  $sA$  model,  $g_\chi/g_q = 1$ , mono- $Z$  channel.

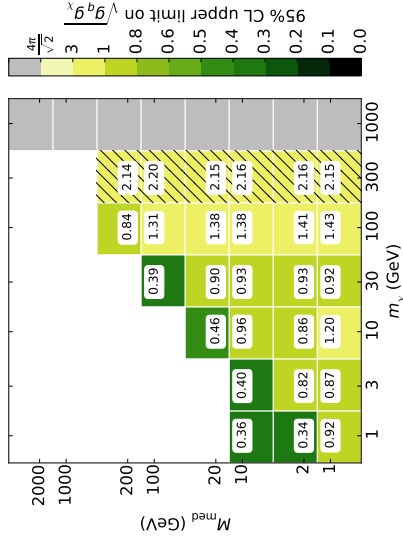


(f)  $sA$  model,  $g_\chi/g_q = 1$ , mono- $W/Z$  channel.

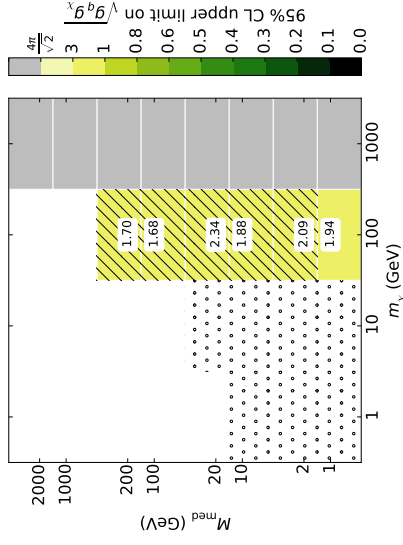
**Figure 4:** Upper limits on the couplings for the  $s$ -channel models in the mono-jet (left), mono- $Z$ (lep) (centre) and mono- $W/Z$ (had) (right) channels, for  $g_\chi/g_q = 1$ . Refer to fig. 3 for details.



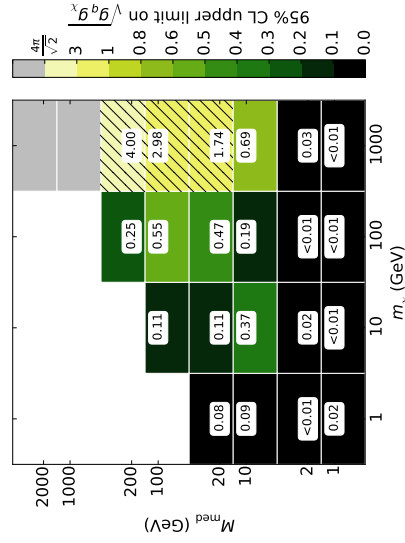
(a)  $sV$  model,  $g_\chi/g_q = 2$ , mono-jet channel.



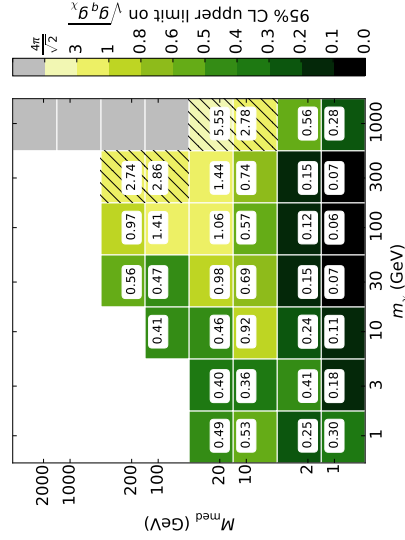
(b)  $sV$  model,  $g_\chi/g_q = 2$ , mono- $Z$  channel.



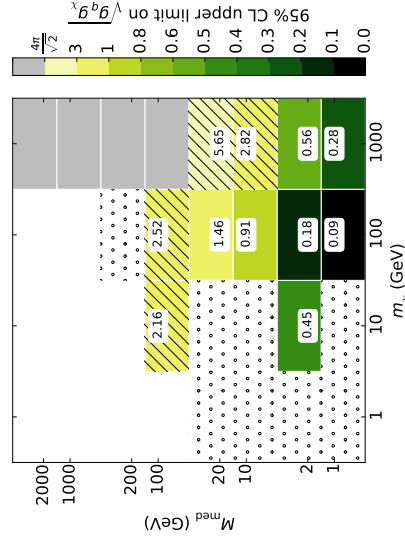
(c)  $sV$  model,  $g_\chi/g_q = 2$ , mono- $W/Z$  channel.



(d)  $sA$  model,  $g_\chi/g_q = 2$ , mono-jet channel.

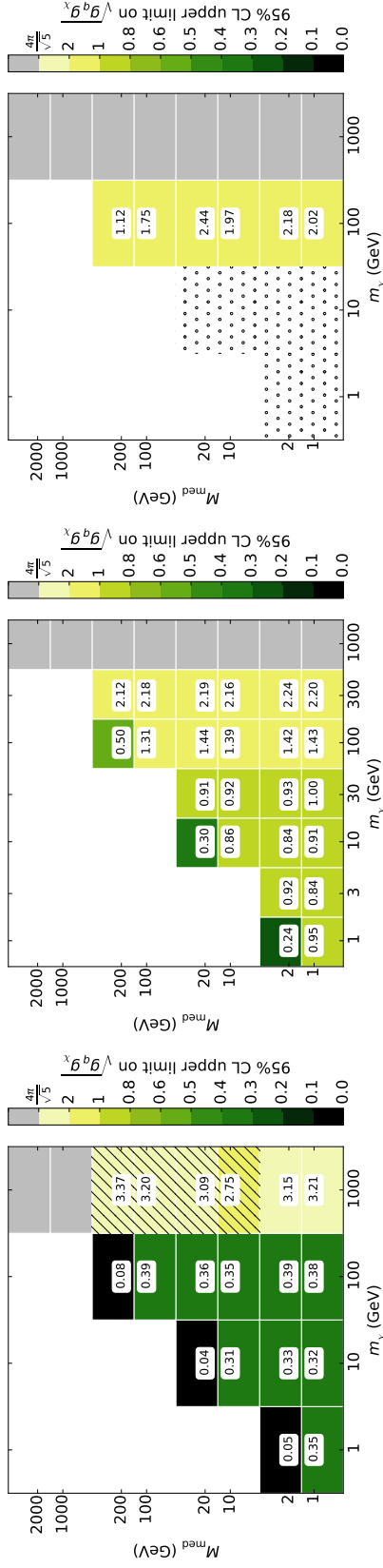


(e)  $sA$  model,  $g_\chi/g_q = 2$ , mono- $Z$  channel.

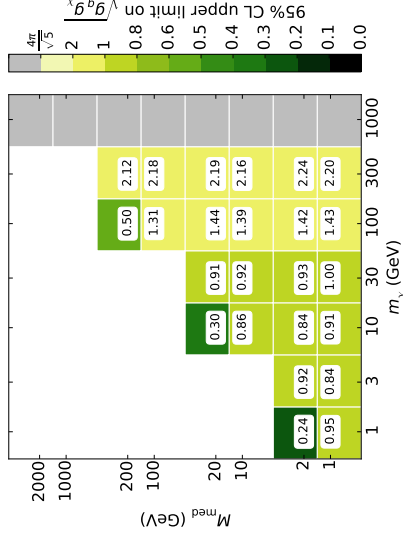


(f)  $sA$  model,  $g_\chi/g_q = 2$ , mono- $W/Z$  channel.

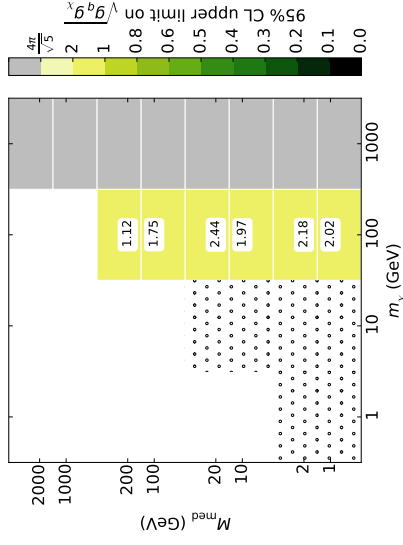
**Figure 5:** Upper limits on the coupling for the  $s$ -channel models in the mono-jet (left), mono- $Z$ (lep) (centre) and mono- $W/Z$ (had) (right) channels, for  $g_\chi/g_q = 2$ . Refer to fig. 3 for details.



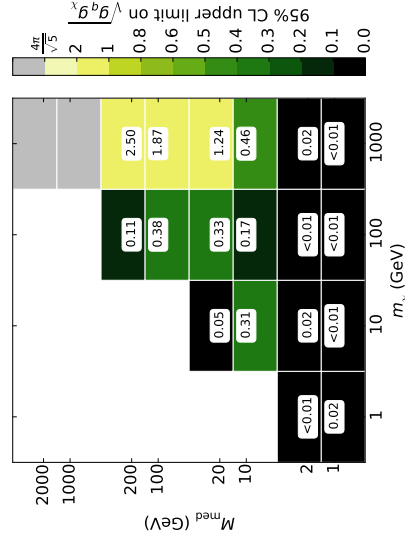
(a)  $sV$  model,  $g_\chi/g_q = 5$ , mono-jet channel.



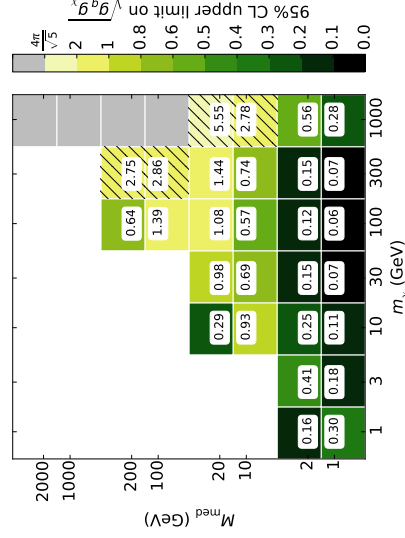
(b)  $sV$  model,  $g_\chi/g_q = 5$ , mono- $Z$  channel.



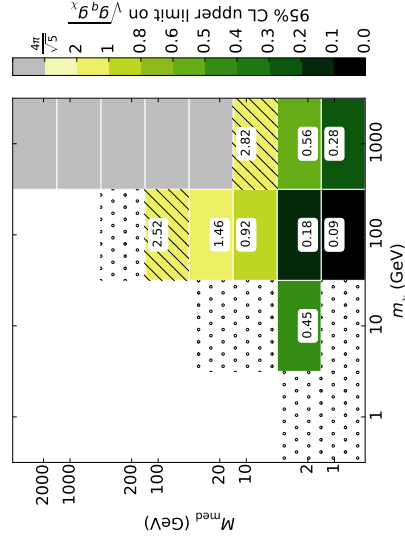
(c)  $sV$  model,  $g_\chi/g_q = 5$ , mono- $W/Z$  channel.



(d)  $sA$  model,  $g_\chi/g_q = 5$ , mono-jet channel.



(e)  $sA$  model,  $g_\chi/g_q = 5$ , mono- $Z$  channel.



(f)  $sA$  model,  $g_\chi/g_q = 5$ , mono- $W/Z$  channel.

**Figure 6:** Upper limits on the coupling for the  $s$ -channel models in the mono-jet (left), mono- $Z$ (lep) (centre) and mono- $W/Z$ (had) (right) channels, for  $g_\chi/g_q = 5$ . Refer to fig. 3 for details.

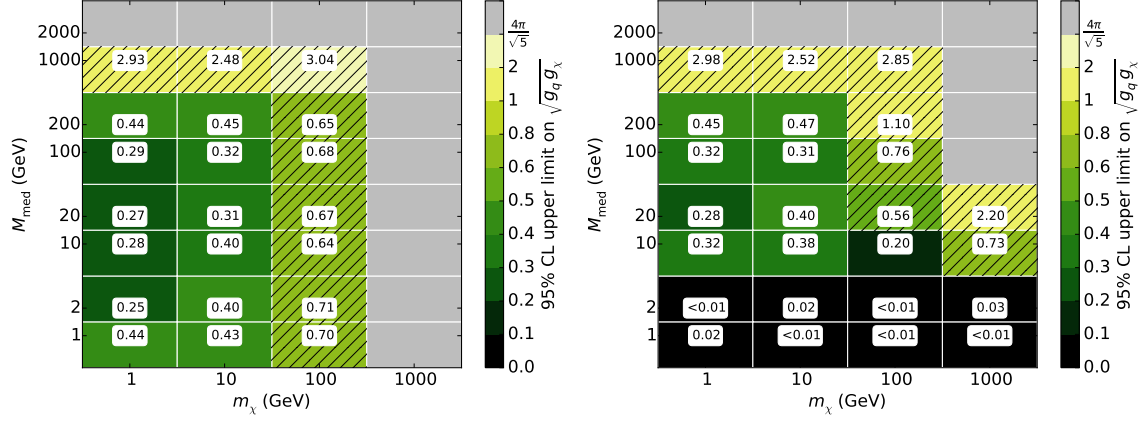


**Figure 7:** Upper limits on the coupling for the  $s$ -channel models in the mono-jet channel, for  $g_\chi/g_q = 0.2$ . Refer to fig. 3 for details.

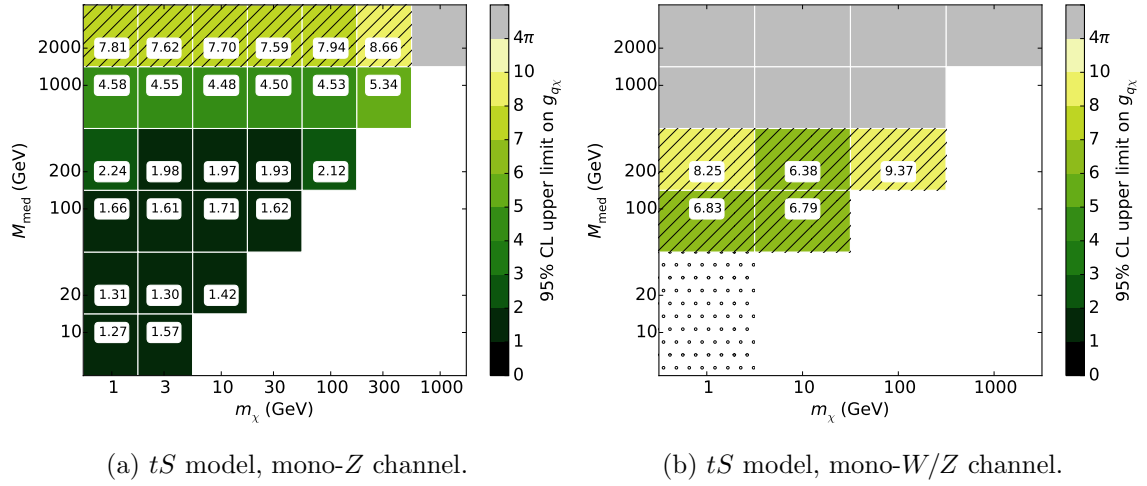


**Figure 8:** Upper limits on the coupling  $g_{q\chi}$  for the  $t$ -channel model in the mono- $Z$ (lep) (left) and mono- $W/Z$ (had) (right) channels. Refer to fig. 3 for details.

435 In this scenario, the measured abundance is approximately related to the unknown  
 436 self-annihilation cross-section via

$$\Omega_{\text{DM}} h^2 \simeq \frac{2 \times 2.4 \times 10^{-10} \text{ GeV}^{-2}}{\langle \sigma v \rangle_{\text{ann}}}. \quad (4.1)$$

437 This is used with measurements of the DM abundance by Planck,  $\Omega_{\text{DM}}^{\text{obs}} h^2 = 0.1199 \pm$   
 438  $0.0027$  [36], to find  $\langle \sigma v \rangle_{\text{ann}} \simeq 4.0 \times 10^{-9} \text{ GeV}^{-2}$  for thermal relic DM. This relation is  
 439 only approximately accurate, and so we use the micrOMEGAs code [52] to determine the  
 440 coupling strength leading to the correct relic density for each model. We verified this  
 441 technique against the semi-analytic technique outlined in e.g. ref. [37].

442 If the DM mass lies at the electroweak scale, the thermal relic scenario provides a  
 443 natural explanation for the observed DM density, and so the coupling strengths leading to  
 444 the correct relic density are a natural benchmark with which to compare constraints from  
 445 other DM searches, indicating the scale at which we expect the couplings may lie. However  
 446 the relic density couplings should by no means be treated as a constraint. If the DM was  
 447 not produced thermally or if there is some unknown effect which modifies the evolution of  
 448 the density with temperature, then these relations break down. Further, even if DM is a  
 449 thermal relic, then the relationship no longer holds if there are other annihilation channels  
 450 not taken into account, or if there are other beyond-SM particles contributing to the DM  
 451 abundance.

### 452 4.3 Comparison with Direct Detection Constraints

453 In Figs. ?? we also show the intercept line where constraints from direct detection exper-  
 454 iments are equally as strong as the LHC constraint. Below and to the right of the dotted  
 455 line, direct detection constraints are stronger than the LHC constraint, while above and  
 456 to the left, the LHC gives the stronger constraint. We use the toolset from Ref. [?] to  
 457 convert the strongest available direct detection constraints, which are from the LUX 2013  
 458 dataset [?], onto constraints on our models.

459 Compared to direct detection, the LHC performs relatively better for the SAD model  
 460 than for the SVD model. This is because the axial-vector coupling leads to a suppressed  
 461 scattering rate in direct detection experiments while the LHC is relatively insensitive to  
 462 the difference between the vector and axial-vector couplings. In the non-relativistic limit,  
 463 the TSD model leads to a mix of both suppressed and unsuppressed operators.

464 The direct detection constraints assume that the DM candidate under consideration  
 465 contributes 100% of the local DM density, while the LHC constraints make no assumptions  
 466 about either the local DM density or overall abundance. In this sense the LHC constraints  
 467 remain useful even in the region where they are not as strong as those from direct detection.

### 468 4.4 Discussion

- 469 • Comparison to direct mediator searches: dijet gives strongest constraints on mediator  
 470 especially for small  $r$ . Missing ET still good for large  $M$  but in this region EFT is  
 471 fine

- Comparison to non-grid searches, e.g. McCullough et al
- Comparison to grid searches e.g. Zurek et al, Jacques and Nordstrom

## 5 Conclusion

MonoX searches dominate.

## 6 Acknowledgements

### A Limit setting strategy

In this appendix we present a summary of the procedure employed to calculate the 95% confidence level (CL) limits on the coupling parameter  $\sqrt{g_q g_\chi}$ , where this parameter can be replaced with  $g_{q\chi}$  for the  $tS$  model, and  $M_\star$  in the validation of the mono-jet analysis.

#### A.1 Nominal Values

For each SiM, the nominal limit is calculated by taking the model-independent upper limit on  $\sigma \times \mathcal{A} \times \epsilon$  from each analysis, dividing by the value of  $\mathcal{A} \times \epsilon$  (which is taken as a single parameter for each point) to obtain the limiting cross section  $\sigma_{\text{lim}}$ , and rearranging eq. 2.7 to convert to a limit on the couplings. In the  $s$ -channel on-shell case, the width can be expressed as a function of  $g_q$  and the ratio  $g_\chi/g_q$ , which simplifies the calculation. We arrive at

$$\sqrt{g_q g_{\chi\text{lim}}} = \begin{cases} \sqrt{g_q g_{\chi\text{gen}}} \times (\sigma_{\text{lim}}/\sigma_{\text{gen}})^{\frac{1}{2}} & \text{if } M_{\text{med}} \geq 2m_{\text{DM}} \text{ (} s\text{-channel)} \\ \sqrt{g_q g_{\chi\text{gen}}} \times (\sigma_{\text{lim}}/\sigma_{\text{gen}})^{\frac{1}{4}} & \text{if } M_{\text{med}} < 2m_{\text{DM}} \end{cases} \quad (\text{A.1})$$

where  $\sqrt{g_q g_{\chi\text{gen}}}$  and  $\sigma_{\text{gen}}$  are the input couplings and cross-section (taken from PYTHIA 8), respectively.

The signal region in each case is chosen based on where the best ‘expected’ limit lies, where that limit is calculated assuming that exactly the expected SM background is observed.

#### A.2 Uncertainty Estimation

Our nominal limits rely on both  $\sigma_{\text{gen}}$  and  $\mathcal{A} \times \epsilon$  and so are subject to systematic uncertainties which derive from our choice of signal generation procedure. For our signal samples, there are three key sources of systematic uncertainty: the factorisation and renormalisation scales, the strong coupling constant ( $\alpha_s$ ) and the choice of parton distribution function (PDF).

We assess the impact of the factorisation and renormalisation default scales in a straightforward manner; by varying them simultaneously by factors of 2 (‘up’) and 0.5 (‘down’). The systematic effects of the strong coupling constant and PDF are difficult to separate and so are treated in tandem. We assume that the systematic uncertainty introduced

main systematic sources	PDF/tune	factorisation and renormalisation scales	matching scale (mono-jet only)
variation ‘up’	NNPDF2.1LO + Monash tune	2	160 GeV
nominal	MSTW2008lo68cl + ATLAS UE AU2-MSTW2008LO	1	80 GeV
variation ‘down’	CTEQ6L1 + ATLAS UE AU2-CTEQ6L1	0.5	40 GeV

**Table 5:** Reading left to right, the sources of systematic uncertainty considered in this analysis. Each point in phase space is varied up or down by one of these sources, and the systematic uncertainty is then taken from the resultant changes to the acceptance and cross-section in comparison to their nominal values.

by  $\alpha_s$  at matrix-element level is negligible when compared to the PDF uncertainties, as demonstrated to be valid in ref. [42]. The variation of  $\alpha_s$  in conjunction with a change of PDF is done with the use of specific tunes in PYTHIA 8, which we change simultaneously with the PDF choice to estimate the uncertainty on  $\Delta\sigma_{gen}$ . The nominal choices of PDF and tune are varied ‘up’ to NNPDF2.1LO PDF + Monash tune, and ‘down’ to CTEQ6L1 PDF and ATLAS UE AU2-CTEQ6L1 tune. For the mono-jet channel, the impact of the matching scale (QCUT) is assessed in a manner similar to that of the factorisation and renormalisation scales. That is, we vary the QCUT by factors of 2 (‘up’ to 160 GeV) and 0.5 (‘down’ to 40 GeV). These systematic uncertainty sources are summarised in table 5.

The average variation in the nominal value of  $\sigma_{lim}$  (measured as a fraction of  $\sigma_{lim}$ ) resulting from each systematic source is added in quadrature and propagated to  $\sqrt{g_q g_\chi}$  to obtain the total systematic uncertainty. This process is adjusted slightly to account for the inclusion of statistical uncertainties, which are estimated conservatively by taking the 95% CL *lower* limit on  $\mathcal{A} \times \epsilon$  as calculated with the Wald approximation, i.e.  $\mathcal{A} \times \epsilon \rightarrow (\mathcal{A} \times \epsilon) - \Delta(\mathcal{A} \times \epsilon)$ . Note that the uncertainty on the luminosity is less than 3%, so is considered to be negligible in comparison to other systematic sources.

## B Validation of signal simulation and event selection procedures

### B.1 Monojet Channel

The signal generation and selection procedures for the mono-jet channel are validated via reproduction of the ATLAS limits on  $M_\star \equiv M_{med}/\sqrt{g_q g_\chi}$ , for the  $s$ -channel vector SiM. A

comparison of SR7<sup>8</sup> limits for a representative sample of mediator masses with  $m_\chi = 50$  GeV,  $\Gamma = M/8\pi$  and  $\sqrt{g_q g_\chi} = 1$  is presented in Table 6. In general, good agreement is observed between the ATLAS and reproduced limits, with a maximum difference of 12%. We note that a discrepancy of a few percent is expected given the differences in signal simulation. For example, the simplified matching procedure discussed in detail in Sec 3.1.1 introduces an additional uncertainty of approximately 25% for events with  $E_T^{\text{miss}} > 350$  GeV when compared to the approach utilised by the ATLAS mono-jet group. Further uncertainties are introduced by the jet smearing approximation used in place of a full detector simulation and by the 95% CL estimation procedure (outlined in Appendix A) used instead of a thorough HistFitter treatment. As our results are consistently more conservative than those of the ATLAS analysis, we consider our approach to be acceptable.

$M_\star^{\text{gen}}$ [TeV]	$M_\star^{95}$ [GeV] (ATLAS)	$M_\star^{95}$ [GeV] (this work)	Difference [%]
0.05	91	89	2.16
0.3	1151	1041	7.3
0.6	1868	1535	11.8
1	2225	1732	12.0
3	1349	1072	6.8
6	945	769	8.5
10	928	724	10.6
30	914	722	9.6

**Table 6:** Comparison of the 95% CL upper limits on  $M_\star$  from this work and from the ATLAS mono-jet analysis [41]. The limits are compared for an  $s$ -channel model with  $m_\chi = 50$  GeV and  $\Gamma$  set to a fixed value of  $M_{\text{med}}/8\pi$ , for the process  $pp \rightarrow \chi\bar{\chi} + 1, 2j$  with QCUT = 80 GeV. Note that  $M_\star^{\text{gen}}$  is the input suppression scale.

## B.2 Mono- $Z(\text{lep})$ Channel

The ATLAS mono- $Z(\text{lep})$  results include an upper limit on the coupling  $g_{q\chi}$  for a  $t$ -channel SiM analogous to our  $tS$  model, and so it is this model which we use to validate our signal generation and selection procedures. Note that the following differences exist: the ATLAS model includes just two mediators ( $up$ - and  $down$ -type) where we consider six, the DM particle is taken to be Majorana where we assume Dirac, and the couplings  $g_{t,b\chi}$  are set to zero where we have universal coupling to all three quark generations.

Table 7 shows the 95% CL upper limits on  $g_{q\chi}$  that we calculate using our own generation procedure (and the values in table 3), compared with the limits taken from the ATLAS analysis. Also shown is the difference as a percentage of the ATLAS limit. We see reasonable agreement; most of the 11 points in parameter space are within 10% of the ATLAS limits, and all are within 26%. Additionally, our results are consistently more

<sup>8</sup>We use this signal region as it is the only one for which ATLAS limits are provided.



$m_\chi$ [GeV]	$M_{\text{med}}$ [GeV]	$g_{q\chi}^{95\%CL}$ (ATLAS)	$g_{q\chi}^{95\%CL}$ (this work)	Difference [%]
10	200	1.9	2.0	5.3
	500	2.8	3.2	14.3
	700	3.5	4.4	25.7
	1000	4.5	5.2	15.6
200	500	3.4	4.0	17.6
	700	4.2	4.5	7.1
	1000	5.2	5.3	1.9
400	500	5.5	5.7	3.6
	700	6.1	6.5	6.6
	1000	7.2	7.4	2.8
1000	1200	23.3	24.1	3.4

**Table 7:** Comparison of the upper limit on  $g_{q\chi}$  from the ATLAS analysis [47] and this work.

conservative, which again is to be expected given the less sophisticated nature of our generation procedure. As in the case of the mono-jet validation, the differences stem from the use of  $p_T$  smearing applied to the leptons (rather than a full reconstruction simulation) and from the simplified treatment of systematics; we also obtained  $\sigma \times \mathcal{A} \times \epsilon$  independently.

### B.3 Mono- $W/Z$ (had) Channel

The event generation and selection procedures for the mono- $W/Z$ (had) channel are validated via reproduction of the ATLAS limit on  $M_\star$  for the D9 EFT operator with  $m_\chi = 1$  GeV. We see agreement within 7.4%, with the ATLAS limit being the stronger of the two. This is to be expected for several reasons. In addition to those reasons already stated in sections B.1 and B.2, the ATLAS analysis uses a shape fit to extract their limit while we use a cut-and-count approach. Furthermore, the ATLAS limit is quoted at 90% CL, while ours is calculated at 95% CL. The agreement of limits on  $M_\star$  was also verified for the D5 EFT operator. The ATLAS mono- $W/Z$ (had) analysis only published the limits for D5 in the low- $E_T^{\text{miss}}$  signal region, whereas we use the high- $E_T^{\text{miss}}$  signal region in our recast. Hence, a larger discrepancy than for D9 is expected. We found an agreement within 12.5%, showing that the limits obtained from the two different signal regions are not very far apart and hence our strategy of focusing only on the high- $E_T^{\text{miss}}$  signal region is clearly suboptimal but not by much. Natives :) feel free to rephrase!

## References

- [1] ATLAS Collaboration, *Search for new phenomena with the monojet and missing transverse momentum signature using the ATLAS detector in  $\sqrt{s} = 7$  TeV proton-proton collisions*, *Phys. Lett. B* (2011), arXiv:1106.5327.

EFT operator	$m_\chi$ [GeV]	$M_\star^{90\%CL}$ [GeV] (ATLAS)	$M_\star^{95\%CL}$ [GeV] (this work)	Difference [%]
D9	1	2400	2221	7.4
D5	1	570	499	12.5

**Table 8:** Comparison of the upper limit on  $M_\star$  from the ATLAS mono- $W/Z$ (had) analysis [48] and this work.

- [2] ATLAS Collaboration, *Search for New Phenomena in Monojet plus Missing Transverse Momentum Final States using  $10 \text{ fb}^{-1}$  of  $pp$  collisions at  $\sqrt{s}=8 \text{ TeV}$  with the ATLAS detector at the LHC*, 2012, ATLAS-CONF-2012-147.
- [3] CMS Collaboration, *Search for new physics in monojet events in  $pp$  collisions at  $\sqrt{s} = 8 \text{ TeV}$* , 2013, CMS-PAS-EXO-12-048.
- [4] M. R. Buckley, *Using Effective Operators to Understand CoGeNT and CDMS-Si*, *Phys.Rev. D* 88, 055028 (2013), arXiv:1308.4146.
- [5] ATLAS Collaboration, *Search for new phenomena with mono-jet plus missing transverse energy signature in  $pp$  collisions at  $\sqrt{s}=8 \text{ TeV}$  with the ATLAS detector*, 2012, ATL-COM-PHYS-2012-1211.
- [6] N. Bell et al., *Searching for Dark Matter at the LHC with a Mono-Z*, *Phys.Rev. D* 86, 096011 (2012), arXiv:1209.0231.
- [7] N. Zhou, D. Berge, and D. Whiteson, *Mono-everything: combined limits on dark matter production at colliders from multiple final states*, *Phys.Rev. D* 87, 095013 (2013), arXiv:1302.3619.
- [8] M. Cahill-Rowley et al., *Complementarity and Searches for Dark Matter in the  $pMSSM$* , SLAC-PUB-15450 (2013), arXiv:1305.6921.
- [9] ATLAS Collaboration, *Further search for supersymmetry at  $\sqrt{s} = 7 \text{ TeV}$  in final states with jets, missing transverse momentum and isolated leptons with the ATLAS detector*, *Phys.Rev. D* 86, 092002 (2012), arXiv:1208.4688.
- [10] ATLAS Collaboration, *Search for squarks and gluinos with the ATLAS detector in final states with jets and missing transverse momentum using  $4.7 \text{ fb}^{-1}$  of  $\sqrt{s} = 7 \text{ TeV}$  proton-proton collision data*, *Phys.Rev. D* 87, 012008 (2013), arXiv:1208.0949.
- [11] ATLAS Collaboration, *Search for pair-produced third-generation squarks decaying via charm quarks or in compressed supersymmetric scenarios in  $pp$  collisions at  $\sqrt{s} = 8 \text{ TeV}$  with the ATLAS detector*, *Phys.Rev. D* 90, 052008 (2014), arXiv:1407.0608.
- [12] ATLAS Collaboration, *Search for squarks and gluinos with the ATLAS detector in final states with jets and missing transverse momentum using  $\sqrt{s} = 8 \text{ TeV}$  proton-proton collision data*, *JHEP* 09 (2014) 146, arXiv:1405.7875.
- [13] H. Dreiner et al., *Contact Interactions Probe Effective Dark Matter Models at the LHC*, *Europhys.Lett.* (2013), arXiv:1303.3348.
- [14] J. Goodman et al., *Gamma Ray Line Constraints on Effective Theories of Dark Matter*, *Nucl.Phys.* (2011), arXiv:1009.0008.

- [15] G. Busoni et al., *On the Validity of the Effective Field Theory for Dark Matter Searches at the LHC*, *Phys.Lett.* (2014), arXiv:1307.2253.
- [16] G. Busoni et al., *On the Validity of the Effective Field Theory for Dark Matter Searches at the LHC, Part II: Complete Analysis for the s-channel*, *JCAP* 1406:060 (2014), arXiv:1402.1275.
- [17] G. Busoni et al., *On the Validity of the Effective Field Theory for Dark Matter Searches at the LHC Part III: Analysis for the t-channel*, *JCAP* 09 (2014) 022, arXiv:1405.3101.
- [18] Oliver Buchmueller, Matthew J. Dolan, Sarah A. Malik and Christopher McCabe, *Characterising dark matter searches at colliders and direct detection experiments: Vector mediators*, 2014, arXiv:1407.8257.
- [19] J. Kumar and D. Marfatia. *Matrix element analyses of dark matter scattering and annihilation*, *Phys.Rev.* (2013), arXiv:1305.1611.
- [20] G. Jungman et al., *Supersymmetric dark matter*, *Phys.Rept.* (1996).
- [21] P. J. Fox et al., *Missing Energy Signatures of Dark Matter at the LHC*, *Phys.Rev.* (2012), arXiv:1109.4398.
- [22] P. J. Fox, R. Harnik, R. Primulando, and C-T. Yu, *Taking a Razor to Dark Matter Parameter Space at the LHC*, *Phys.Rev.* (2012), arXiv:1203.1662.
- [23] M. Papucci, A. Vichi, and K. M. Zurek, *Monojet versus rest of the world I: t-channel Models*, *JHEP* (2014), arXiv:1402.2285.
- [24] Y. Bai, P. J. Fox, and R. Harnik, *The Tevatron at the Frontier of Dark Matter Direct Detection*, *JHEP* (2010), arXiv:1005.3797.
- [25] J. Goodman et al., *Constraints on Dark Matter from Colliders*, *Phys.Rev. D* 82, 116010 (2010), arXiv:1008.1783.
- [26] P. J. Fox, R. Harnik, J. Kopp, and Y. Tsai, *LEP Shines Light on Dark Matter*, *Phys.Rev.* (2011), arXiv:1103.0240.
- [27] M. L. Graesser, I. M. Shoemaker, and L. Vecchi, *A Dark Force for Baryons*, 2011, arXiv:1107.2666.
- [28] H. An and F. Gao, *Fitting CoGeNT Modulation with an Inelastic, Isopin-Violating  $Z'$  Model*, 2011, arXiv:1108.3943.
- [29] CMS Collaboration, *Search for narrow resonances using the dijet mass spectrum in pp collisions at  $\sqrt{s} = 8\text{TeV}$* , *Phys.Rev.* (2013), arXiv:1302.4794.
- [30] ATLAS Collaboration, *Search for high-mass resonances decaying to dilepton final states in pp collisions at  $\sqrt{s} = 7\text{-TeV}$  with the ATLAS detector*, *JHEP* (2012), arXiv:1209.2535.
- [31] P. Harris, V. V. Khoze, M. Spannowsky and C. Williams, *Constraining Dark Sectors at Colliders: Beyond the Effective Theory Approach*, *Phys.Rev.* (2015), arXiv:1411.0535.
- [32] CMS Collaboration. *Search for new physics in monojet events in pp collisions at  $\sqrt{s} = 8\text{TeV}$* , 2013, CMS-PAS-EXO-12-048.
- [33] ATLAS Collaboration. *Search for New Phenomena in Monojet plus Missing Transverse Momentum Final States using  $10\text{fb}^{-1}$  of pp collisions at  $\sqrt{s} = 8\text{TeV}$  with the ATLAS detector at the LHC*, 2012, ATLAS-CONF-2012-147.

- [34] J. Kumar and D. Marfatia, *Matrix element analyses of dark matter scattering and annihilation*, *Phys.Rev.* (2013), arXiv:1305.1611.
- [35] D. Alves et al., *Simplified Models for LHC New Physics Searches*, *J.Phys.* (2012), arXiv:1105.2838.
- [36] P. A. R. Ade *et al.* [Planck Collaboration], *Astron. Astrophys.* **571**, A16 (2014) [arXiv:1303.5076 [astro-ph.CO]].
- [37] G. Busoni, A. De Simone, T. Jacques, E. Morgante and A. Riotto, *Making the Most of the Relic Density for Dark Matter Searches at the LHC 14 TeV Run*, *JCAP* 03 (2015) 022, arXiv:1410.7409.
- [38] CMS Collaboration. *Search for new physics in monojet events in pp collisions at  $\sqrt{s} = 8$  TeV*, 2013, CMS-PAS-EXO-12-048.
- [39] ATLAS Collaboration. *Search for New Phenomena in Monojet plus Missing Transverse Momentum Final States using 10 fb<sup>1</sup> of pp collisions at  $\sqrt{s} = 8$  TeV with the ATLAS detector at the LHC*, 2012, ATLAS-CONF-2012-147.
- [40] ATLAS Collaboration. *Further search for supersymmetry at  $\sqrt{s} = 7$  TeV in final states with jets, missing transverse momentum and isolated leptons with the ATLAS detector*, *Phys.Rev.* (2012), arXiv:1208.4688.
- [41] ATLAS Collaboration. *Search for new phenomena in final states with an energetic jet and large missing transverse momentum in pp collisions at  $\sqrt{s} = 8$  TeV with the ATLAS detector*, 2015, arXiv:1502.01518
- [42] S. Schramm, *Searching for Dark Matter with the ATLAS Detector in Events with an Energetic Jet and Large Missing Transverse Momentum*, 2015, CERN-THESIS-2015-038.
- [43] A. Cooper-Sarkar. *PDFs for the LHC*, 2011, arXiv:1107.5170.
- [44] ATLAS Collaboration. *Search for dark matter candidates and large extra dimensions in events with a jet and missing transverse momentum with the ATLAS detector*, 2013, CERN-PH-EP-2012-210, arXiv:1210.4491.
- [45] P. J. Fox et al. *Missing Energy Signatures of Dark Matter at the LHC*, *Phys. Rev.*, 2012.
- [46] N. Bell, J. Dent, T. Jacques, and T. Weiler. *W/Z Bremsstrahlung as the Dominant Annihilation Channel for Dark Matter*, *Phys. Rev.*, 2011.
- [47] ATLAS Collaboration. *Search for dark matter in events with a Z boson and missing transverse momentum in pp collisions at  $\sqrt{s} = 8$  TeV with the ATLAS detector*, *Phys.Rev.D* **90** (2014) 012004, arXiv:1404.0051.
- [48] ATLAS Collaboration. *Search for dark matter in events with a hadronically decaying W or Z boson and missing transverse momentum in pp collisions at  $\sqrt{s} = 8$  TeV with the ATLAS detector*, *Phys. Rev. Lett.* **112** (2014) 041802, arXiv:1309.4017.
- [49] J. Alwall /emphet al.. *The automated computation of tree-level and next-to-leading order differential cross sections, and their matching to parton shower simulations*, *JHEP07* (2014) 079, arXiv:1405.0301.
- [50] A. D. Martin, W. J. Stirling, R. S. Thorne, G. Watt, *Parton distributions for the LHC*, *Eur.Phys.J.C63*, (2009), 189-285, arXiv:0901.0002.
- [51] ATLAS Collaboration. *Summary of ATLAS Pythia8 tunes*, 2012, ATL-PHYS-PUB-2012-003.

- [52] G. Blanger, F. Boudjema, A. Pukhov and A. Semenov, *Comput. Phys. Commun.* **192**, 322 (2015) doi:10.1016/j.cpc.2015.03.003 [arXiv:1407.6129 [hep-ph]].
- [53] D. Abercrombie et al. *Dark Matter Benchmark Models for Early LHC Run-2 Searches: Report of the ATLAS/CMS Dark Matter Forum*, arXiv:1507.00966.
- [54] M. Baak et al. *HistFitter software framework for statistical data analysis*, *Eur.Phys.J.C* (2015), arXiv:1410.1280.
- [55] J. Abdallah et al. *Simplified Models for Dark Matter Searches at the LHC*, *Phys. Dark Uni.* 9-10 (2015) 8-23, arXiv:1506.03116.
- [56] J. Abdallah et al. *Simplified Models for Dark Matter and Missing Energy Searches at the LHC*, (2014), arXiv:1409.2893.
- [57] T. Jacques and K. Nordstrom, *Mapping monojet constraints onto Simplified Dark Matter Models*, *JHEP* 06 (2015) 142, arXiv:1502.05721.
- [58] T. Sjstrand et al. *An Introduction to PYTHIA 8.2*, *Comput. Phys. Comm.* 191 (2015) 159-177, arXiv:1410.3012.
- [59] R. M. Godbole, G. Mendiratta and T. M. P. Tait, *A Simplified Model for Dark Matter Interacting Primarily with Gluons*, *JHEP* 08 (2015) 064, arXiv:1506.01408.
- [60] ATLAS Collaboration, *Search for dark matter produced in association with a hadronically decaying vector boson in pp collisions at  $\sqrt{s} = 13$  TeV with the ATLAS detector at the LHC*, ATLAS-CONF-2015-080 (2015).
- [61] M. L. Mangano et al. *Matching matrix elements and shower evolution for top-quark production in hadronic collisions*, *JHEP* 01 (2007), hep-ph/0611129.
- [62] ATLAS Collaboration, *Performance of jet substructure techniques for large- $R$  jets in proton-proton collisions at  $\sqrt{s} = 7$  TeV using the ATLAS detector*, *JHEP* 09 (2013) 076, arXiv:1306.4945.
- [63] M. Cacciari, G. P. Salam and G. Soyez, *FastJet user manual*, arXiv:1111.6097.
- [64] N. F. Bell et al, *Dark matter at the LHC: EFTs and gauge invariance*, *Phys. Rev. D* 92 (2015) 053008, arXiv:1503.07874.